

# Mapping Complex Myoarchitecture in the Bovine Tongue with Diffusion-Spectrum Magnetic Resonance Imaging

Richard J. Gilbert, Lee H. Magnusson, Vitaly J. Napadow, Thomas Benner, Ruopeng Wang, and Van J. Wedeen  
Department of Mechanical Engineering, Massachusetts Institute of Technology, Cambridge, Massachusetts; and Athinoula A. Martinos Imaging Center, Department of Radiology, Massachusetts General Hospital, Boston, Massachusetts

**ABSTRACT** The ability to resolve complex fiber populations in muscular tissues is important for relating tissue structure with mechanical function. To address this issue in the case of tongue, we employed diffusion spectrum imaging (DSI), an MRI method for determining three-dimensional myoarchitecture where myofiber populations are variably aligned. By specifically varying gradient field strength, molecular displacement in a tissue can be determined by Fourier-transforming the echo intensity against gradient strength at fixed gradient pulse spacing. The displacement profiles are visualized by graphing three-dimensional isocontour icons for each voxel, with the isocontour shape and size representing the magnitude and direction of the constituting fiber populations. To validate this method, we simulated a DSI experiment within the constraints of arbitrary crossing fibers, and determined that DSI accurately depicts the angular relationships between these fibers. Considering the fiber relationships in the whole bovine tongue, we compared the images obtained by DSI with those obtained by diffusion tensor imaging in an anterior slice of the lingual core, a region known to possess extensive fiber crossing. In contrast to diffusion tensor imaging, which depicts the anterior core solely as a region with low anisotropy due to the presence of mixed-orientation fiber populations, DSI shows two distinct fiber populations, with an explicit orthogonal relationship to each other. In imaging the whole lingual tissue, we discerned arrays of crossing and noncrossing fibers involving the intrinsic and extrinsic muscles, which merged at regions of interface. We conclude that DSI has the capacity to determine three-dimensional fiber orientation in structurally complex muscular tissues.

## INTRODUCTION

In the course of normal speech and swallowing, the human tongue is required to assume a large number of shapes, positions, and degrees of stiffness (1–5). It is generally believed that the structural basis of the tongue's mechanical virtuosity is its extensively interwoven myoarchitecture, whereby the constituting myofibers are simultaneously aligned along multiple spatial axes at the microscopic scale. The precise determination of the tongue's myoarchitecture and the relationship of its myoarchitecture to mechanical function are questions that have long challenged students of biological mechanics.

From an anatomical perspective, the tongue consists of an overlapping three-dimensional network of skeletal muscle fibers and fiber bundles, involving both intrinsic fibers, i.e., those fibers possessing no direct connection to bony surfaces, and extrinsic fibers, i.e., those fibers possessing connections to bony surfaces (6–10). The intrinsic musculature consists of a core region of orthogonally aligned fibers, contained within a sheathlike tract of longitudinally oriented fibers. The intrinsic fibers are delicately merged with extrinsic muscles that modify shape and position from a superior (palatoglossus), posterior (styloglossus), and inferior (genioglossus and hyoglossus) direction. The fact that the intrinsic and extrinsic fibers appear to merge structurally along

several geometric planes opens to question the classical anatomical distinction between “intrinsic” and “extrinsic” fibers, and suggests that the lingual myoarchitecture may more appropriately be considered as a continuum of variably oriented fibers. The demonstration of continuous properties in the setting of biological tissues requires a method for determining muscle fiber alignment along multiple planes and spatial scales in intact structures.

Tissue imaging modalities, such as ultrasound, x-ray CT, and conventional MRI pulse sequences, do not have the capacity to resolve intramural fiber organization. On the other hand, NMR imaging of proton diffusivity has the capacity to infer fiber direction *in situ* based on the extent of direction-specific MR signal attenuation (11–14). The concept of Q-space has been proposed as a method to conceptualize how such diffusion data might be used to portray complex microscopic structures, and specifically provides a method for indexing a set of diffusion-weighted images (15–18). Q-space imaging uses the Fourier transform relationship to derive the probability density function (PDF) for spin displacement from the motion-dependent attenuation of the diffusion signal, with the assumption that biological barriers create directionally specific dissimilarities in molecular diffusion. A simplified form of diffusion-weighted imaging, diffusion tensor imaging (DTI) has been employed to resolve fiber orientation in excised sheep and cow tongues (19–21) as well as other tissues, such as the heart (22–27) and the brain (28–30). DTI data are generally depicted in terms of the principal fiber direction (principal eigenvector) of the

---

*Submitted June 13, 2005, and accepted for publication March 17, 2006.*

Address reprint requests to Richard J. Gilbert, MD, Dept. of Mechanical Engineering, Massachusetts Institute of Technology, 77 Massachusetts Ave., Cambridge, MA 02139. Tel.: 617-620-2032; Fax: 781-622-5090. E-mail: rgilbert@mit.edu.

© 2006 by the Biophysical Society

0006-3495/06/08/1014/09 \$2.00

---

doi: 10.1529/biophysj.105.068015

constituting myofibers, and the degree to which local fibers are homogeneously or heterogeneously aligned (diffusion anisotropy). Although DTI is accurate in delineating fiber direction for regions of homogeneous fiber alignment (parallel at the scale of the voxel), it has limited accuracy for determining fiber alignment when presented with more complex intravoxel patterns, such as fiber crossing or divergence. DTI is further limited in that it assumes that intravoxel diffusion follows a Gaussian model and that fluid exchange across restrictive membranes is relatively slow.

To accurately track molecular diffusion in multiple directions, more robust diffusion methods are required. Accordingly, several novel diffusion-based MR methods have been described, namely high-angular resolution diffusion, (31,32) higher-order tensor, (33,34) Q-ball, (35–37), and diffusion spectrum imaging (DSI) (38,39). We describe here a novel application of DSI for quantifying the alignment of structurally complex muscle fiber populations in the tongue, for which the complete three-dimensional spin displacement function per voxel is determined. This approach involves the acquisition of numerous diffusion-weighted MR images per voxel, each with a different diffusion-weighting gradient value and angularity. The extension of such methods to other organs, characterized by higher order complexity, should elucidate principles by which heterogeneous microstructures contribute to macroscale patterns of deformation in biological tissue.

## METHODS

### DSI of myofiber populations

Diffusion is a physical property that represents the random translational motion of water molecules in tissue and is principally affected by the location of diffusional barriers, membrane permeability, bulk motion, temperature, and magnetic susceptibility. If there are no macromolecular barriers to affect water movement in a tissue preparation, molecular diffusion is equal in all directions. In contrast, when diffusion is hindered by the existence of macromolecular barriers (i.e., membranes or fibers), the pattern of molecular motion is greater along preferred directions. It is this preferential motion in the direction of myofibers that allows one to deduce three-dimensional myoarchitecture from net molecular diffusion. Since myocytes are cylindrically symmetric, their elongated cellular membranes impose barriers for the self-diffusion of free water. Thus, maximal signal attenuation occurs preferentially along the long axis of the myofiber. By combining the signal attenuation obtained via the application of diffusion-weighting gradients in multiple directions with standard MRI image acquisition, the amount of diffusion in those directions may be measured for each voxel and then reconstructed to constitute three-dimensional representations of tissue myoarchitecture.

Diffusion spectrum imaging (DSI) is a method for determining the average amount of molecular diffusion occurring within any enclosed space, such as the set of myofibers within a given segment of tissue. The goal of DSI is to reconstruct the PDF for diffusion in each voxel. DSI accomplishes this by acquiring a full sampling of diffusion-weighting gradient directions and magnitudes, which permits direct reconstruction of the average PDF. In DSI, diffusion-weighted images are acquired for a sphere of  $\mathbf{q}$  vectors with indexed values in a Cartesian grid in  $q$ -space, to produce a three-dimensional probability distribution. The relationship between the diffusion attenuation and a diffusion-weighting gradient  $\mathbf{g}$  of duration  $\delta$  is depicted by:

$$M(\mathbf{q}, \Delta) = M(\mathbf{0}, \Delta) \int \bar{P}_s(\mathbf{R}|\Delta) \exp(i\mathbf{q} \cdot \mathbf{R}) d\mathbf{R} \quad (1)$$

$$\mathbf{q} = \gamma \mathbf{g} \delta,$$

where  $\mathbf{q}$  is called the  $q$ -value,  $\gamma$  is the proton gyromagnetic ratio for a water molecule,  $M$  is the signal intensity,  $\Delta$  is the diffusion time,  $\mathbf{R}$  is the diffusion distance, and  $\bar{P}_s$  is the average PDF. In DSI, diffusion-weighted images are acquired for a sphere of  $\mathbf{q}$  vectors with indexed values in a Cartesian grid in  $q$ -space, to produce a three-dimensional probability distribution. The PDF  $\bar{P}(\mathbf{R}, \Delta)$  is the inverse Fourier transform of Eq. 1:

$$\bar{P}_s(\mathbf{R}, \Delta) = F^{-1}[M(\mathbf{q}, \Delta)], \quad (2)$$

where  $F^{-1}$  denotes the inverse Fourier transform. The spacing between  $\mathbf{q}$  vectors defines the field of view and the maximum  $\mathbf{q}$  vector defines the resolution of the PDF. The values of  $M(\mathbf{q}, \Delta)$  are placed in a matrix with indices given by the indices of the  $\mathbf{q}$  vectors, and the three-dimensional inverse discrete Fourier transform is computed, producing the PDF. By measuring the microscopically resolved three-dimensional diffusion functions, DSI resolves the multi-modal behavior of the PDF within a macroscopically resolved voxel of tissue.

To achieve practical  $q$ -space imaging, DSI modifies the pulse sequence to include noninfinite pulse width (38,39). If Gaussian conditions are assumed during constant gradient application, then the diffusion time in the above equations is replaced with an effective diffusion time

$$\Delta_e = \Delta - \delta/3. \quad (3)$$

Since Gaussian diffusion cannot be assumed during  $\delta$  for most biological systems, we represent the diffusion data with the center-of-mass (COM) diffusion propagator formalism (40), which accounts for the fact that nonrandom molecular displacements occur during the duration of  $\delta$ .

The three-dimensional diffusion propagator represents a spatial volume and it is necessary to reduce it in dimensions to make visualization more clear. The method typically employed in DSI is to integrate  $\bar{P}_s$  weighted radially by the magnitude of  $\mathbf{R}$ :

$$\text{ODF}(\mathbf{u}) = \int \bar{P}_s(\rho\mathbf{u}) \rho u d\rho, \quad (4)$$

where  $\mathbf{u}$  is a unit vector in the direction of  $\mathbf{R}$ . This produces a probability distribution that is a function only of fiber angle and is weighted to better show long diffusion distances. This new data set is termed the orientational distribution function (ODF) and provides a probability distribution for diffusion for a set of angular directions, weighted by the magnitude of the diffusion. To further simplify visualization, the ODF is normalized by subtracting the smallest magnitude value from the entire distribution. The ODF is plotted with colors corresponding to direction and magnitude, and radii are defined by the values of the ODF.  $q$ -space and standard  $k$ -space imaging are combined by taking a  $k$ -space image for each point in  $q$ -space, thus resulting in a separate diffusion propagator result for each voxel in the  $k$ -space image.

### Simulation of diffusion propagator function in muscle-fiber-like environment

Since diffusion imaging of myofibers is based on the assumption that maximum free diffusion occurs parallel to fiber direction (and is considerably more restricted in the direction perpendicular to the fibers), the presence of two equally distributed populations of muscle fibers with different orientations in a particular voxel should result in two diffusion maxima in two different directions. The average diffusion propagator is a unique data set closely related to fiber orientations for the muscle tissue in a voxel. Although the average diffusion propagator is not equivalent to the underlying structure (i.e., proton density  $\rho(\mathbf{r})$ ), it provides a reasonable

approximation of fiber orientations. There are two important cases of the average diffusion propagator, one is the average diffusion propagator ( $\bar{P}_S$ ) corresponding to the actual molecular motion that takes place on the timescale of a DSI experiment, and the second is the COM average diffusion propagator (see above), which accounts for molecular motion during the course of finite pulse-width gradients.

Since analytic solutions involving complex structures and boundary conditions are not feasible, we performed finite-element simulations to assess the behavior of these diffusion propagators. Since skeletal muscle is composed of directional bundles of muscle fibers, skeletal myofibers may be considered as aligned, fluid-filled cylinders surrounded by extracellular fluid and represented by an orientational vector. Although analysis of such myoarchitecture requires a complex multi-compartmented model, one can approximate the diffusion environment by assuming that the muscle fiber bundles permit water molecules composing the intra- and extracellular fluid to diffuse preferentially in the direction of the fiber bundles. Preferential diffusion is the basis of the diffusion signal in which a local maximum direction of anisotropic diffusion correlates directly to the direction of the fibers in that region. For purposes of the current simulation, only two-dimensional shapes were considered. The spatial scaling is in the order of normal skeletal muscle fibers, that is, 20  $\mu\text{m}$  in width and 200  $\mu\text{m}$  in length.

We performed finite-element simulations of the behavior of a diffusion propagator for a set of model crossing fibers. The general finite-element simulation was constructed and solved (MATLAB Partial Differential Equation Toolbox, MathWorks, Natick, MA) using the following diffusion equation, which was determined for each element:

$$\frac{\partial P_S(\mathbf{R}, \mathbf{r})}{\partial t} = D \nabla^2 P_S(\mathbf{R}, \mathbf{r}), \quad (5)$$

with  $D$  as a constant isotropic diffusion term and  $P_S(\mathbf{R}, \mathbf{r})$  is the diffusion propagator (i.e., the probability distribution of spins having diffused a distance  $\mathbf{R}$  given the initial condition  $\mathbf{r}$ ). This equation was used in two dimensions with zero-flux Neumann boundary conditions. The mesh was automatically generated using the supplied tool. The simulation was then iterated for each point in the mesh, applying a  $\delta$ -function initial condition at a unique mesh point per iteration. Each simulation solved for the transient diffusive behavior occurring around its particular mesh point  $\delta$ -function.

The complete data set, derived in this manner, was processed into the format that would be obtained from an actual NMR diffusion imaging scan. This format was obtained by applying simulated, time-dependent, directional diffusion gradients in the same way as would occur during an MRI scan. Specifically, the MR gradients produce a spatially dependent phase change based on the distance and direction  $\mathbf{R}$  of diffusion from the starting point  $\delta$ -function to the surrounding mesh points, given by the  $\mathbf{q} \cdot \mathbf{R}$  term in Eq. 1. The signal magnitude at the surrounding mesh points is proportional to concentration at that mesh point. In this manner, each mesh point has a phase and a signal magnitude for each gradient applied. The magnitudes and phases were summed three times, first over all the mesh points in a simulation iteration, second over all the simulation iterations, and finally over the discrete time points in the simulation, applying first  $+\mathbf{q}$  for  $\delta$ , then no gradients for  $\Delta$ , then  $-\mathbf{q}$  for another  $\delta$ , similar to the procedure employed in an actual MR scan. These summed signal magnitudes and phases were calculated for several different diffusion gradient magnitudes and directions, thus simulating  $q$ -space data acquisition.

## Magnetic resonance imaging protocol

For imaging the bovine tongue, diffusion-weighted imaging was applied to the entire tissue; the data set acquired was processed using both weighted least-square-error DTI and DSI. Magnetic resonance imaging was performed on three ex vivo cow tongues obtained from Blood Farm (West Groton, MA). The tongues were obtained by making an incision from the thyroid prominence to the angle of the mandible to expose the tongue, followed by en bloc resection. Whole-tongue specimens were refrigerated and scanned within 24 h of harvest.

Diffusion-weighted data were acquired from contiguous axial and sagittal slices at 1.5T with a 20-cm receive-transmit head coil and a diffusion-sensitive echo planar imaging pulse sequence. The diffusion weighted imaging protocol employed a diffusion-gradient sampling scheme, which consisted of a key-hole Cartesian acquisition to include  $q$ -space values lying on a Cartesian grid ( $q$  spacing = 0.06  $\mu\text{m}^{-1}$ ) within a sphere of radius  $q_{\text{max}} = 0.3 \mu\text{m}^{-1}$ , for a total of 515 sampling points. This sampling scheme provided a diffusion spectrum resolution of 3  $\mu\text{m}$  and a field of view of 30  $\mu\text{m}$ . The imaging parameters were  $TE/TR = 88/2800$  ms, a  $64 \times 64 \times 25$  imaging grid, with resolutions of ((2.8 mm) (3) – (4 mm) (3)), and  $b$ -values of 4500–8500  $\text{s}/\text{mm}^2$ .

Explicit comparison of the imaging outcome of DSI and DTI was performed for the same imaging slice of the tongue, an anterior axial slice in which crossing intrinsic fibers are present, employing the full raw data set obtained from the diffusion-weighted experiment described above. DTI constitutes a weighted least-square-error solution of the Gaussian diffusion tensor model to the entire set of diffusion-weighted images (13). The least-square-error weighting is provided by the error covariance matrix for the natural log calculation used to make the signal attenuation function linear. By assuming Gaussian diffusion, the signal attenuation data set should correlate to

$$M(\mathbf{q}, \Delta) = M(\mathbf{0}, \Delta) \cdot e^{(-\mathbf{q}^T \mathbf{D}^{\text{eff}} \mathbf{q}) \Delta_e}, \quad (6)$$

where  $\mathbf{D}^{\text{eff}}$  is the effective, or observed, diffusion tensor. The complete three-dimensional diffusion tensor was computed for each voxel and visualized as an octahedron whose axes were scaled by the size of the eigenvalues and oriented along the corresponding eigenvectors. For each octahedron, the principal eigenvector corresponded to the direction of greatest diffusion, or the principal fiber direction, whereas the eigenvalues and eigenvectors for each diffusion tensor represented the magnitude and direction of maximal proton diffusivity, respectively. Comparison was made regarding the ability of each method to discern angular relationships among the principal fiber populations existing in individual voxels.

## RESULTS

### Simulation of diffusion propagator behavior in the setting of model crossing fibers

We performed simulations to assess the behavior of the diffusion propagator in the setting of model two-dimensional crossing-fiber populations with a communicating intracellular space (Fig. 1 A). For this simulation, a simpler subset than that employed in the above methods was used. The simulation was repeated for each of the mesh points, with each simulation having a different mesh point  $\delta$ -function initial condition at  $\mathbf{r}$ . The results for each of the mesh point initial-condition simulations were then centered with the  $\delta$ -function at zero and interpolated on a rectangular grid and summed for just a single time point. This computes the average diffusion propagator  $\bar{P}_S$ , which is the sum of probability density functions  $P_S(\mathbf{R}, \mathbf{r})$  for all possible initial positions ( $\mathbf{r}$ ) within the structure, assuming a constant molecular density distribution. The computed average diffusion propagator is shown in Fig. 1 B at  $t = 500$  ms. The value of the average diffusion propagator is greatest in the center due to the fact that molecules have the greatest probability of remaining around their origin and that molecules are inherently limited in the number of directions they can diffuse from their origin. Also shown are peaks protruding from its center that relate to the known

fiber directions. The diffusion peaks drop off quickly because longer diffusion distances become improbable. The resulting ODF was calculated with Eq. 4 and provided coloring and radius values corresponding to its values (Fig. 1 C).

### Simulation of a prototypical DSI experiment

Fig. 1 D shows the extension of the above simulation to include a DSI pulse sequence and the Fourier transform reconstruction. The spins acquire spatially dependent phase shifts from magnetic field gradients as specified by Eq. 1. The gradients applied correspond to a keyhole Cartesian grid of  $\mathbf{q}$  vectors. For each  $\mathbf{q}$  vector, the phase acquired for each mesh point  $\delta$ -function initial condition is calculated by using the pulsed gradient applied at several different discrete simulation time steps, and summed across time as described in Methods. The values of the gradients applied are positive  $\mathbf{q}$  for  $0 < t < \delta$ , zero for  $\delta < t < \Delta$ , and negative  $\mathbf{q}$  for  $\Delta < t < \Delta + \delta$ . The resulting phases for all mesh point simulations are then summed together with Eq. 3, resulting in the signal for that value of  $\mathbf{q}$ . The signal values obtained fill a two-dimensional array indexed by  $\mathbf{q}$ . The two-dimensional discrete Fourier transform is calculated, resulting in the COM average diffusion propagator shown in Fig. 1 D. This propagator has similar features to the average diffusion propagator except that it possesses beneficial sharpening of its peaks. The ODF is shown with a superimposed DTI solution (calculated with Eq. 5) for this simulation (Fig. 1 E), confirming the inability of DTI to accurately resolve the angularity of crossing fibers.

### Comparison of DSI with DTI representations for a single coronal bovine tongue slice

The principal limitation of DTI in resolving the fibers of the anterior core of the tongue is the inability to determine the relative orientation of fibers existing in oblique directions to each other in the setting of a microscale voxel. DTI is thus limited to a determination of the plane of greatest angular dispersion, where two or more myofiber populations exist. In contrast, we considered that DSI would allow us to visualize directly all fiber populations, and thereby permit us to quantify fiber relationships. We depict in Fig. 2 a set of diffusion images of an axial imaging slice through the anterior bovine tongue (intact excised tissue), with the data displayed both in the form of DTI (Fig. 2 A) and DSI (Fig. 2 B). The DTI data demonstrate individual diffusion tensors in the form of octahedra, whose axes were scaled according to the magnitude of the eigenvalues and oriented along the corresponding eigenvectors. The eigenvalues and eigenvectors for each tensor represent the magnitude and direction of maximal diffusivity, respectively. The array of fibers within the voxel may thus be represented in terms of degrees of anisotropy. The DSI data demonstrated distinct fiber population heterogeneity in the anterior tongue. The longitudinal sheath was present on the periphery as a single through-plane fiber population, whereas the tongue core exhibited both transversus and verticalis myofiber populations. Inferior voxels again showed the existence of only a single fiber population, most likely the extrinsic genioglossus muscle fanning superiorly into the tongue body. We specifically compared the individual voxel depictions of the crossing and noncrossing

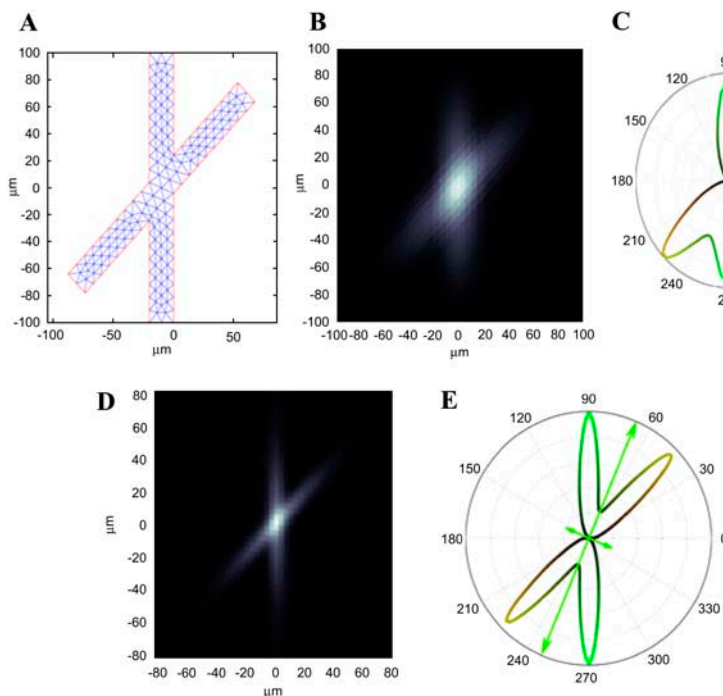


FIGURE 1 Finite-element simulation for diffusion imaging of model crossing fibers. Finite-element simulations were obtained to portray the behavior of a diffusion propagator for a simple set of two-dimensional crossing fibers with communicating water, employing water diffusion at  $t = 500$  ms and isotropic water diffusion coefficient  $D = 2.5 \times 10^3 \mu\text{m}^2/\text{s}$ . (A) Automatically generated finite-element mesh with 189 points depicting realistic geometry of size and angular relationship for crossing skeletal muscle fibers. (B) Image depicting the average diffusion propagator  $\bar{P}$  computed from the simulation. (C) Radially weighted ODF computed from the image in D. (D) Simulation of an actual DSI experiment employing the crossing-fiber model shown in A. A finite-pulse-width PGSE sequence was simulated with  $\delta = 350$  ms,  $\Delta = 600$  ms, and a 10-mT/m maximum gradient strength. The resulting diffusion propagator obtained from the simulation is shown. This propagator is physically interpretable as the COM propagator. (E) Radially weighted ODF superimposed on the eigenvectors calculated from the simulation data using a DTI approach. The maximum DTI eigenvector is limited to bisecting the two simulated fibers.

lingual core fibers. These images demonstrate, in the case of DTI, a characteristic octahedron associated with a low anisotropy condition (indicating relatively equal populations of fibers in oblique directions to each other, but not designating their angular relationship), and in the case of DSI, a characteristic image depicting explicitly the principal-fiber-crossing-fiber populations with an orthogonal relationship (Fig. 2 C).

### Demonstration of crossing and noncrossing fiber populations in the intact lingual tissue

We demonstrate in Fig. 3 a single midsagittal imaging slice of the bovine tongue obtained by DSI and viewed as a set of ODFs color-coded relative to direction. These images show that specific regions demonstrate that constituting fibers are either homogeneously aligned per voxel, i.e., noncrossing pattern (Fig. 3, C and D) or heterogeneously aligned, i.e., crossing pattern (Fig. 3 D). These patterns are distinguished by the presence (Fig. 3 D) or absence (Fig. 3, B and C) of a prominent transverse (*blue*) fiber component. At the interface between regions, there is evidence of an intricate merging of these fiber alignment patterns, so that nominally discrete muscle populations are not discernible. Rather regions are delineated with varying degrees of fiber crossing or noncrossing. We demonstrate in Fig. 4 variations in the patterns exhibited by crossing fibers in the anterior core of the tongue in three adjacent axial imaging slices (Fig. 4, A–C). Fig. 4 D

depicts a single voxel at high magnification showing the convergence of three fiber populations, oriented principally in the vertical, transverse, and longitudinal directions. Fig. 4 E depicts a single population of fibers, aligned at an angle between the longitudinal and the vertical, therefore embodying in the  $q$ -space icon elements of both green and red. Fig. 4 F demonstrates two crossing-fiber populations, oriented orthogonal to each other in the vertical and transverse directions. It is presumed that the extent to which crossing fibers are present in a given region impacts upon *its* ability to undergo hydrostatic deformation.

### DISCUSSION

The human tongue is a versatile, lithe, and structurally complex muscular organ that is of paramount importance for performing physiological tasks such as deglutition (swallowing) and phonation (speech). A central question regarding the tongue, which has engaged muscle biologists for hundreds of years, is how does the tissue achieve the myriad degrees of freedom needed to carry out its biological roles (41,42). The extent to which lingual deformation is dictated by its myoarchitecture, defined as the organization of the various muscular elements, provides an opportunity to explore fundamental concepts of structure and function in the broader biological realm. We describe an NMR metric, diffusion spectrum imaging, by which the three-dimensional spatial

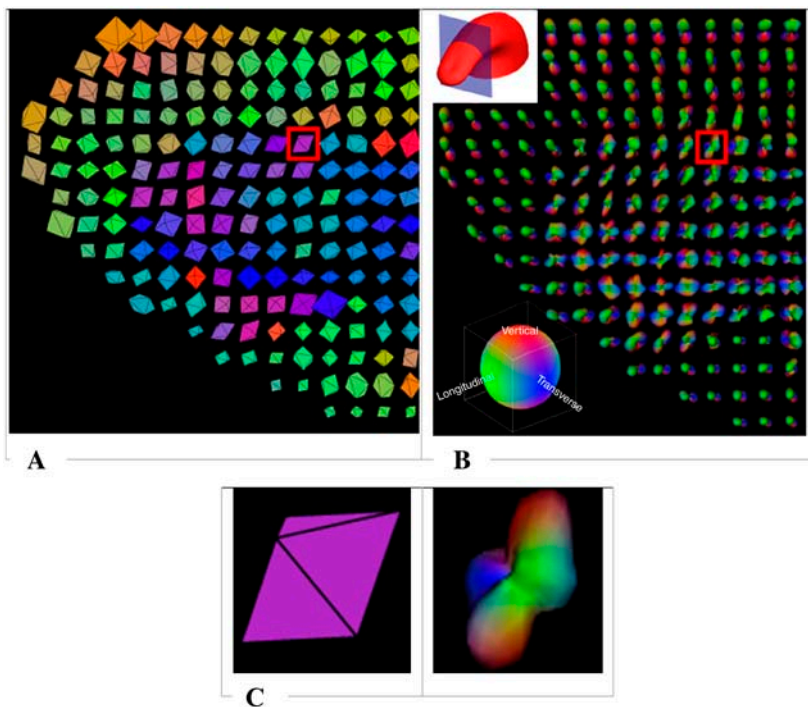


FIGURE 2 Comparison of diffusion-weighted images (DTI, DSI) from an axial bovine tongue slice. Shown are diffusion images obtained from an anterior axial slice in the intact and excised bovine tongue employing both DTI (A) and DSI (B) methods of acquisition and analysis on the same data set. Principal fiber directions are color-coded (*inset*), with green indicating the tissue's longitudinal axis, red the vertical axis, and blue the transverse axis. (A) DTI data constituting a weighted least-squares solution of the Gaussian diffusion tensor model. The complete three-dimensional diffusion tensor was computed for each voxel and visualized as octahedra whose axes were scaled by the size of the eigenvalues and oriented along the corresponding eigenvectors. (B) DSI data obtained using the pulse sequence herein for tissue specific  $q$ -space imaging. Comparison is made of individual voxel icons obtained using either DTI or DSI from regions of the anterior tongue slice where the muscle fibers are homogeneously aligned, i.e., absence of crossing fibers, and from regions of the tongue slice where the fibers are heterogeneously aligned, i.e., possesses crossing fibers. (C) Isolated voxel containing crossing fibers depicted as both DTI icon and DSI ODF. The DTI data set demonstrates a characteristic octahedron, whose non-extended shape indicates a low anisotropy condition. This is consistent with the presence of equal populations of fibers in oblique relationship to each other, but does not designate the presence of multiple fiber populations or define an explicit angular relationship. In contrast, DSI demonstrates orthogonal crossing-fiber populations by the explicit shape of the ODF.

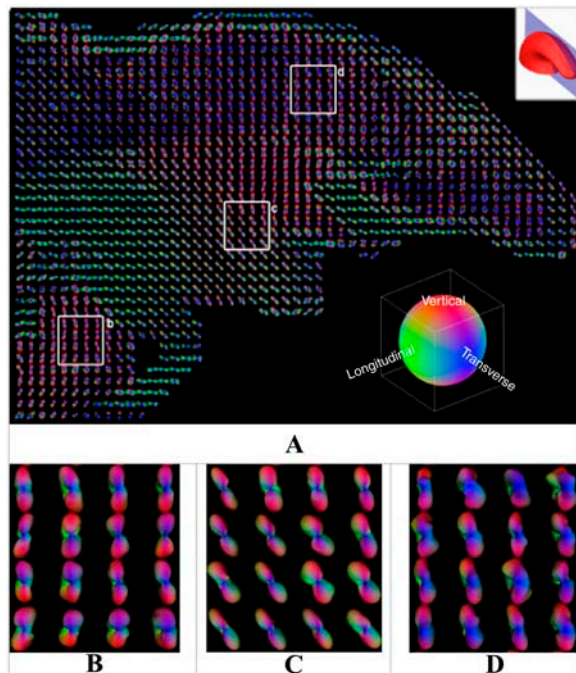


FIGURE 3 Midsagittal diffusion-spectrum imaging slice obtained from the bovine tongue. (A) Midsagittal imaging slice of the bovine tongue obtained by DSI and depicted as a set of three-dimensional ODFs. Principal fiber directions are color-coded (*inset*), with green indicating the tissue's longitudinal axis, red the vertical axis, and blue the transverse axis. (B–D) Whole sagittal slice, with principal fiber populations color-coded in the vertical (*red*), transverse (*blue*), and longitudinal (*green*) directions. Selected regions are shown at increased magnification to discern ODF detail: (B) single vertically-oriented parallel fiber population; (C) single diverging fiber population, principally in the vertical orientation; and (D) crossing-fiber populations in the core of the tongue, with fibers in the vertical (*red*) and transverse (*blue*, out of page) directions.

relationships existing among the crossing and noncrossing fibers of the tongue, and potentially other complex tissues, may be determined.

In this study, we first demonstrated the validity of using DSI for characterizing model crossing fibers by simulating the behavior of the average diffusion propagator and a prototypical DSI experiment. The average diffusion propagator is a unique data set closely related to the sum of diffusive activity for water molecules within a designated segment of tissue, and provides a “snapshot” of the arrays of fiber populations within the voxel. This analysis was then applied for imaging a set of crossing fibers within the core of the anterior portion of the bovine tongue for comparison with DTI, from a single sagittal imaging slice, and from a set of contiguous axial slices derived from the anterior tissue. Our data specifically demonstrates that the tongue tissue may be delineated into regions defined by the degree to which fibers are homogeneously aligned, i.e., without significant crossing-fiber populations at the voxel resolution, or heterogeneously aligned, i.e., exhibiting 2–3 crossing-fiber populations. We further demonstrate that regions exhibiting extensive cross-

ing merge in an almost seamless manner with regions exhibiting homogeneity of fiber alignment, thus reaffirming the concept that the lingual musculature, and perhaps numerous other muscle systems, are best conceived as mechanical continua rather than the simple juxtaposition of discrete muscle populations. The ability of DSI to portray the angular relationships existing among the fiber populations is shown here in the case of the tongue, an instance in which complex geometric arrangements are necessary to achieve the many deformations associated with speech and swallowing.

From a mechanical perspective, the tongue is generally considered to be a form of muscular hydrostat (43–48), an organ whose musculature both creates motion and supplies skeletal support for that motion. As such, it capitalizes on its high water content, and hence incompressibility, to modify its form, without change in volume. By definition, all hydrostats in nature possess fibers parallel and perpendicular to the organ's long axis, but they differ regarding the relative position and geometry of the perpendicular fibers. Although there is much diversity in the animal kingdom regarding the manner in which the tongue manifests its hydrostatic properties, the pervasive morphological construct is the presence of orthogonally aligned set of muscle fibers. The mammalian tongue is, in fact, a unique form of muscular hydrostat, inasmuch as it embodies both intrinsic and extrinsic fibers. In this manner, deformations resulting from contractions of the intrinsic components of the hydrostat may be augmented and modified by extrinsic elements that tether to the surrounding skeletal structure. Synergistic contractions of extrinsic and intrinsic muscles of the tongue, anatomically indistinct at the point of their insertion in the body of the tongue, may thus contribute to hydrostatic deformations. Given the complexity of the tongue's myoarchitecture, these motions may produce a near-infinite number of combinations, involving hydrostatic elongation (with associated tissue stiffening) and displacement, secondary to the activation of intrinsic and directionally specific extrinsic fibers.

To define the *in situ* myoarchitecture of the tongue, we previously employed diffusion tensor imaging methods to interrogate its uncrossed and crossing fiber regions (19–21). In so doing, we were able to resolve the constituent muscles of the tongue based on the principal direction of fibers and the local angular dispersion of these fibers within the imaged element. By this formulation, principal fiber orientation corresponds to the leading eigenvector of the diffusion tensor, whereas the second eigenvector identifies the orientation of maximum fiber-angle dispersion. Through the measure of diffusion anisotropy, a scalar whose magnitude reflects the degree of fiber alignment per voxel, we observed a clear delineation in the anterior tongue between the core fibers, comprised of the orthogonally oriented vertical and transverse muscles (i.e., low anisotropy, uniaxial structures), and the sheath fibers comprised of the longitudinal muscles (i.e., high anisotropy, multi-axial structures). These observations

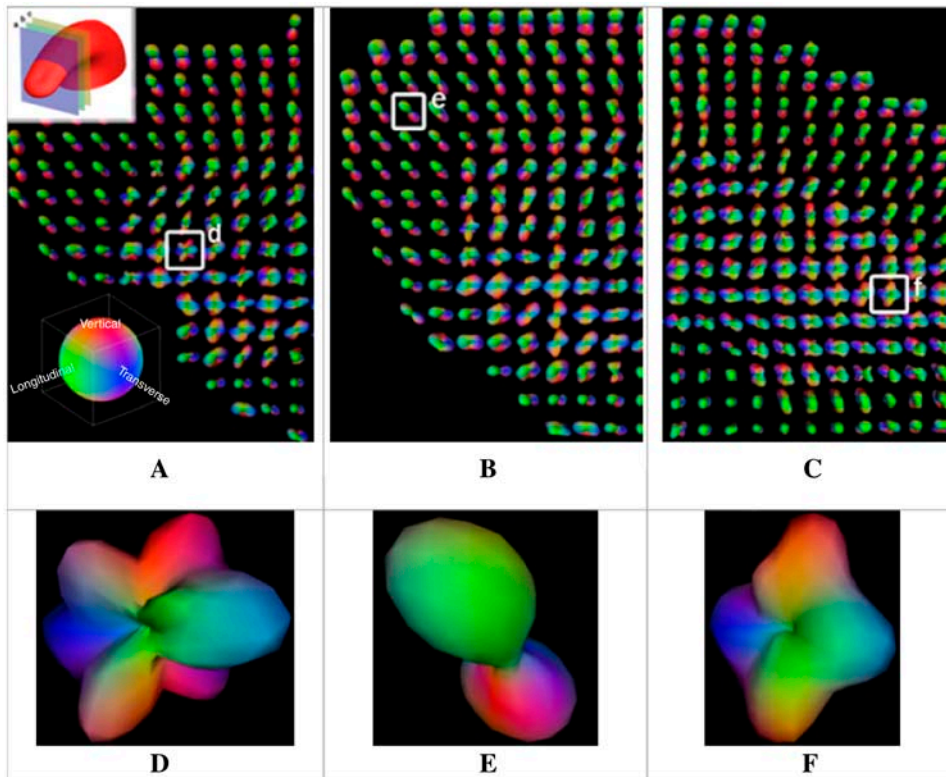


FIGURE 4 (A–C, anterior to posterior) Adjacent axial DSI slices obtained from the bovine tongue and depicted as a set of three-dimensional ODFs. Principal fiber directions are color-coded (*inset*), with green indicating the tissue's longitudinal axis, red the vertical axis, and blue the transverse axis. (D–F) Selected regions of a single voxel at increased magnification to illustrate ODF detail. (D) Single voxel image showing three distinct crossing-fiber populations. (E) Single voxel showing a single population of fibers, oriented diagonally inward toward the tip of the tongue exhibiting longitudinal (*green*) and vertical (*red*) alignment. (F) Single voxel showing two crossing-fiber populations orthogonal to each other.

supported the concept of hydrostatic expansion, by which simultaneous contractions of the vertical and horizontal core muscles cause the tongue (via conservation of volume) to protrude in the anterior-posterior axis at right angles to these fibers. However, relating three-dimensional resolved myoarchitecture of the intrinsic musculature at macroscopic scales (determined by MRI) with its microscopic anatomy (determined by multi-photon microscopy), we observed a fundamental weakness of DTI in quantifying the geometry of fiber populations with a high degree of overlap or convergence. In this instance, the principal eigenvector of the diffusion tensor tends to alternate among several orientations, making the determination of specific fiber orientations ambiguous. Explicit measures of fiber orientation using a single second-order tensor yield a result intermediate between the actual fiber orientations.

The use of DSI may offer several advantages for resolving morphologically complex regions of muscular tissue. DSI, which is based on an NMR depiction of the diffusion propagator formalism, derives an average diffusion function without the requirement of a Gaussian model to describe diffusive behavior. The diffusion propagator defines the probability of a given spin traveling from one position to another in a given diffusion time. DSI yields an ensemble PDF for the set of molecular displacements occurring as a function of molecular motion. Otherwise stated, the PDF indicates the average probability of a spin undergoing a given displacement over a given diffusion time. The PDF for a given diffusion data set

is based on the Fourier relationship between the PDF and the diffusion signal for the spin echo obtained at various gradient strengths. The use of the inverse Fourier transform of the diffusion signal thus allows for the reconstruction of the PDF for a given diffusion data set via formalism termed *q*-space imaging. *q*-Space is simply a method of bookkeeping MRI image acquisitions to enable a complete diffusion propagator reconstruction. The MRI images taken are indexed by their *q*-space value for use in the three-dimensional Fourier transform reconstruction. By measuring the microscopically resolved three-dimensional diffusion function, DSI depicts complex fiber relationships as the multi-modal behavior of the PDF within a macroscopically resolved voxel of tissue.

A postprocessing step for the three-dimensional diffusion function is necessary to make visualization possible in a two-dimensional image. This step transforms the propagator into an ODF with spatially dependent coloring and three-dimensional shaded polygon shapes. The ODF is a transformation of the PDF from Cartesian to spherical coordinates combined with a heuristic for maximizing diffusion contrast, i.e., distinguishing different diffusion modes. The transformation selected for this data set was a conversion to spherical coordinates, followed by radial integration weighted by the diffusion distance. This produced well-defined peaks in the ODF corresponding to maximum diffusion directions. Weighting by the diffusion distance physically relates to attributing more value to spins, which were able to diffuse

over longer distances. This weighting is beneficial also by removing the large isotropic signal at the center of the propagator where there is little spatially dependent contrast.

Given the voxel-scale complexity of the tongue, and the continuous nature of the contractions underlying its deformations, quantifications of the angular relationships involving orthogonally aligned fibers should have value in the derivation of structure-function relationships. In this study, we first demonstrated the capability of the diffusion propagator formalism to reliably depict modeled crossing fibers, then demonstrated the outcome of a prototypical DSI experiment of these same model fibers, showing that explicit angular relationships for the intended fibers can be obtained with this imaging approach. We next demonstrated that DSI could faithfully resolve the orthogonality of the fiber relationships existing within the core region of an axial MR section from an intact bovine tongue. We specifically compared the image output from a DTI and DSI experiment done on the same tissue. These images demonstrate, in the case of DTI, an octahedron whose shape is consistent with the low anisotropy condition, i.e., generally equal populations of fibers oblique to each other, but which does not designate the number of populations or their angular relationship, and for DSI, a graphic identifying the number of principal crossing-fiber populations and their angular relationship. This provides for the first time a method to potentially image the orthogonality of the crossing fibers of the tongue in the intact tissue.

The extension of  $q$ -space imaging into the realm of clinical imaging, although clearly desirable, will embody several technical challenges. As initially conceived,  $q$ -space imaging embodies the application of negligibly short pulses (compared to the interval between pulses, or diffusion time) and rapid rise times. Under these circumstances, the displacement distribution of molecules within the diffusion space is a function of the net displacement of the intended molecules. This allows for the development of the concept of the PDF, which expresses the mean probability of a spin displacement over a given diffusion time. The Fourier relationship between echo magnitude and the PDF allows for the reconstruction of the PDF by applying the inverse Fourier transform of the diffusion MR signal with respect to the molecular displacement wave vector. The use of infinitely short and strong pulses is often associated with the induction of significant eddy currents, which interfere with the imaging gradients and cause image distortions. In addition, typical  $q$ -space acquisition sequences require a gradient strength that may exceed clinical safety standards based on the specific absorption of radiofrequency energy. By its use of finite-length pulses, DSI may constitute a compromise method by which  $q$ -space imaging of muscular tissues may be performed in vivo.

We conclude that the use of DSI distinguishes between regions consisting of crossing and noncrossing fiber populations, and explicitly allows angular quantification of crossing fiber populations. The application of this technique in vivo should allow clinicians to derive measurable assays of

normal and pathological myoarchitecture in anatomically complex tissues without the need for invasive tissue sampling or dissection.

The authors acknowledge the support of grants from the National Institutes of Health to R.J.G. (R01 DC05604) and V.J.W. (R01 MH64044).

## REFERENCES

- Gilbert, R. J., S. Daftary, T. A. Campbell, and R. M. Weisskoff. 1998. Patterns of lingual tissue deformation associated with bolus containment and propulsion during deglutition as determined by echo-planar MRI. *J. Magn. Reson. Imaging*. 8:554–560.
- Miller, A. J. 1982. Deglutition. *Physiol. Rev.* 62:129–184.
- Groher, M. 1997. *Dysphagia: Diagnosis and Management*, 3rd ed. Butterworth-Heinemann Press, Boston.
- Palmer, J. B., N. J. Rudin, G. Lara, and A. W. Crompton. 1992. Coordination of mastication and swallowing. *Dysphagia*. 7:187–200.
- Thexton, A. J. 1992. Mastication and swallowing. *Br. Dent. J.* 173: 197–206.
- Abd-El-Malek, S. 1939. Observations on the morphology of the human tongue. *J. Anat.* 73:201–210.
- Barnwell, Y. M. 1976. Human lingual musculature: an historical review. *Internat. J. Oral Myology*. 2:31–34.
- Miyawaki, K. 1974. A study of the musculature of the human tongue. *Annu. Bull. Res. Inst. Logoped. Phoniatr.* 8:23–50.
- Sonntag, C. F. 1925. The comparative anatomy of the tongues of mammalia. XII. Summary, classification, and physiology. *J. Zool. Proc. Zool Soc. Lond.* 21:701–762.
- Takemoto, H. 2001. Morphological analyses of the human tongue musculature for three-dimensional modeling. *J. Speech Lang. Hear. Res.* 44:95–107.
- Hahn, E. L. 1950. Spin echoes. *Phys. Rev.* 80:580–594.
- Stejskal, E. O. 1965. Use of spin echoes in a pulsed magnetic field gradient to study anisotropic, restricted diffusion and flow. *J. Chem. Phys.* 43:3597–3603.
- Basser, P. J., J. Mattiello, and D. LeBihan. 1994. MR diffusion tensor spectroscopy and imaging. *Biophys. J.* 66:259–267.
- Basser, P. J., and C. Pierpaoli. 1996. Microstructural and physiological features of tissues elucidated by quantitative diffusion tensor MRI. *J. Magn. Reson.* 111:209–211.
- Cory, D. G., and A. N. Garroway. 1990. Measurement of translational displacement probabilities by NMR: an indicator of compartmentation. *Magn. Reson. Med.* 14:435–444.
- Callaghan, P. T. 1993. *Principals of Nuclear Magnetic Resonance Microscopy*. Oxford University Press, Oxford, UK.
- Schaafsma, T. J., A. H. Van, W. D. Palstra, J. E. Snaar, and P. A. de Jager. 1992. Quantitative measurement and imaging of transport processes in plants and porous media by 1H NMR. *Magn. Reson. Imaging*. 10: 827–836.
- Xia, Y., and P. T. Callaghan. 1992. “One-shot” velocity microscopy: NMR imaging of motion using a single phase-encoding step. *Magn. Reson. Med.* 23:138–153.
- Gilbert, R. J., S. Daftary, T. G. Reese, R. M. Weisskoff, and V. J. Wedeen. 1998. Determination of lingual myoarchitecture in whole tissue by NMR imaging of anisotropic water diffusion. *Am. J. Physiol.* 175:G363–G369.
- Wedeen, V. J., T. G. Reese, V. J. Napadow, and R. J. Gilbert. 2001. Demonstration of primary and secondary fiber architecture of the bovine tongue by diffusion tensor magnetic resonance imaging. *Biophys. J.* 80:1024–1028.
- Napadow, V. J., Q. Chen, V. Mai, P. T. C. So, and R. J. Gilbert. 2001. Quantitative analysis of three-dimensionally resolved fiber architecture



- in heterogeneous skeletal muscle tissue using NMR and optical imaging methods. *Biophys. J.* 80:2968–2975.
22. Garrido, L., V. J. Wedeen, K. K. Kwong, U. M. Spencer, and H. L. Kantor. 1994. Anisotropy of water diffusion in the myocardium of the rat. *Circ. Res.* 74:789–793.
  23. Reese, T. G., R. M. Weisskoff, R. N. Smith, B. R. Rosen, R. E. Dinsmore, and V. J. Wedeen. 1995. Imaging myocardial fiber architecture in vivo with magnetic resonance. *Magn. Reson. Med.* 34:786–791.
  24. Hsu, E. W., A. L. Muzikant, S. A. Matulevicius, R. C. Penland, and C. S. Henriquez. 1998. Magnetic resonance myocardial fiber-orientation mapping with direct histological correlation. *Am. J. Physiol.* 274:H1627–H1634.
  25. Hsu, E. W., and C. S. Henriquez. 2001. Myocardial fiber orientation mapping using reduced encoding diffusion tensor imaging. *J. Cardiovasc. Magn. Reson.* 3:339–347.
  26. Panin, V. Y., G. L. Zeng, M. Deffrise, and G. T. Gullberg. 2002. Diffusion tensor MR imaging of principal directions: a tensor tomography approach. *Phys. Med. Biol.* 47:2737–2757.
  27. Tseng, W. Y., V. J. Wedeen, T. G. Reese, R. N. Smith, and E. F. Halpern. 2003. Diffusion tensor MRI of myocardial fibers and sheets: correspondence with visible cut-face texture. *J. Magn. Reson. Imaging.* 17:31–42.
  28. Pierpaoli, C., P. Jezzard, P. J. Basser, A. Barnett, and G. Di Chiro. 1996. Diffusion tensor MR imaging of the human brain. *Radiology.* 201:637–648.
  29. Wiegell, M. R., H. B. Larsson, and V. J. Wedeen. 2000. Fiber crossing in human brain depicted with diffusion tensor MR imaging. *Radiology.* 217:897–903.
  30. Tuch, D. S., V. J. Wedeen, A. M. Dale, J. S. George, and J. W. Belliveau. 2001. Conductivity tensor mapping of the human brain using diffusion tensor MRI. *Proc. Natl. Acad. Sci. USA.* 98:11697–11701.
  31. Tuch, D. S., T. G. Reese, M. R. Wiegell, N. Makris, J. W. Belliveau, and V. J. Wedeen. 2002. High angular resolution diffusion imaging reveals intravoxel white matter fiber heterogeneity. *Magn. Reson. Med.* 48:577–582.
  32. Frank, L. R. 2001. Anisotropy in high angular resolution diffusion-weighted MRI. *Magn. Reson. Med.* 49:935–939.
  33. Liu, C., R. Bammer, B. Acar, and M. E. Moseley. 2004. Characterizing non-Gaussian diffusion by using generalized diffusion tensors. *Magn. Reson. Med.* 51:924–937.
  34. Ozarslan, E., and T. H. Mareci. 2003. Generalized diffusion tensor imaging and analytical relationships between diffusion tensor imaging and high angular resolution diffusion imaging. *Magn. Reson. Med.* 50:955–965.
  35. Tuch, D. S., T. G. Reese, M. R. Wiegell, and V. J. Wedeen. 2003. Diffusion MRI of complex neural architecture. *Neuron.* 40:885–895.
  36. Tuch, D. S. 2004. Q-ball imaging. *Magn. Reson. Med.* 52:1358–1372.
  37. Perrin, M., C. Poupon, B. Rieul, P. Leroux, A. Constantinesco, J. F. Mangin, D. Lebihan. 2005. Validation of *q*-ball imaging with a diffusion fiber crossing phantom on a clinical scanner. *Philos. Trans. R. Soc. Lond. B Biol. Sci.* 360:881–891.
  38. Wedeen, V. J., T. G. Reese, D. S. Tuch, M. R. Wiegell, J.-G. Dou, R. M. Weisskoff, and D. Chessler. 2000. Mapping fiber orientation spectra in cerebral white matter with Fourier-transform diffusion MRI. Presented at the 8th Annual Meeting of the ISMRM, Denver, CO.
  39. Lin, C. P., V. J. Wedeen, J. H. Chen, C. Yao, and W. Y. Tseng. 2003. Validation of diffusion spectrum magnetic resonance imaging with manganese-enhanced rat optic tracts and ex vivo phantoms. *Neuroimage.* 19:482–495.
  40. Wiegell, M. R., D. S. Tuch, H. B. Larsson, and V. J. Wedeen. 2003. Automatic segmentation of thalamic nuclei from diffusion tensor magnetic resonance imaging. *Neuroimage.* 19:391–401.
  41. Mu, L., and I. Sanders. 1999. Neuromuscular organization of the canine tongue. *Anat. Rec.* 256:412–424.
  42. Sawczuk, A., and K. M. Mosier. 2001. Neural control of tongue movement with respect to respiration and swallowing. *Crit. Rev. Oral Biol. Med.* 12:18–37.
  43. Smith, K. K., and W. M. Kier. 1989. Trunks, tongues, and tentacles: moving with skeletons of muscle. *Am. Sci.* 77:29–35.
  44. Kier, W. M., and K. K. Smith. 1985. Tongues, tentacles and trunks: the biomechanics and movement of muscular hydrostats. *Zool. J. Linn. Soc.* 83:307–324.
  45. Nishikawa, K. C., W. M. Kier, and K. K. Smith. 1999. Morphology and mechanics of tongue movement in the African pig-nosed *Hemisis marmoratum*: a muscular hydrostatic model. *J. Exp. Biol.* 202:771–780.
  46. Napadow, V. J., Q. Chen, V. J. Wedeen, and R. J. Gilbert. 1999. Intramural mechanics of the human tongue in association with physiological deformations. *J. Biomech.* 32:1–12.
  47. Napadow, V. J., Q. Chen, V. J. Wedeen, and R. J. Gilbert. 1999. Biomechanical basis for lingual tissue deformation during swallowing. *Am. J. Physiol.* 40:G695–G701.
  48. Napadow, V. J., R. D. Kamm, and R. J. Gilbert. 2002. Biomechanical model of sagittal bending for the human tongue. *J. Biomech. Eng.* 124:547–556.